Rethinking the Ozone-Climate Change Penalty

Xiyue Zhang[1], Darryn W. Waugh[1], Gaige Hunter Kerr[2], and Scot Miller[1]

[1]Johns Hopkins University
[2]The George Washington University

November 21, 2022

Abstract

The daily variation of ground-level ozone (O_3), a harmful pollutant, is positively correlated with air temperature (T) in many midlatitude land regions in the summer. The observed temporal regression slope between O_3 and T is referred to as the "ozone-climate change penalty" and has been proposed as a way to predict the impact of future climate warming on O_3 from observations. Here, we use two chemical transport models to show that the O_3-T correlation is primarily due to the meridional advection of both fields, as opposed to direct temperature-dependent chemistry or emissions. Furthermore, the magnitude of the O_3-T regression (dO_3/dT) can be estimated by the ratio of the time-mean O_3 and T meridional gradients. Consideration of expected changes in the meridional gradients of T and O_3 due to climate change indicates that dO_3/dT will likely change, and caution is needed when using the observed climate penalty to predict O_3 changes.

Rethinking the Ozone-Climate Change Penalty

Xiyue Zhang[1], Darryn W Waugh[1], Gaige Hunter Kerr[2], and Scot M Miller[1,3]

[1]Department of Earth and Planetary Sciences, Johns Hopkins University, Baltimore, Maryland, USA
[2]Department of Environmental and Occupational Health, Milken School of Public Health, George Washington University, Washington, DC, USA
[3]Department of Environmental Health and Engineering, Johns Hopkins University, Baltimore, Maryland, USA

Key Points:

- Transport by meridional advection of O_3 and T explains the spatial variations in daily O_3-T relationship
- Daily regression slope dO_3/dT can be estimated by the ratio of O_3 and T mean meridional gradients when temperature gradients are strong
- Gradient ratio suggests dO_3/dT to change with warming, making it questionable to use observed dO_3/dT in O_3 projection

Corresponding author: Xiyue Zhang, `sallyz@jhu.edu`

Abstract

The daily variation of ground-level ozone (O_3), a harmful pollutant, is positively correlated with air temperature (T) in many midlatitude land regions in the summer. The observed temporal regression slope between O_3 and T is referred to as the "ozone-climate change penalty" and has been proposed as a way to predict the impact of future climate warming on O_3 from observations. Here, we use two chemical transport models to show that the O_3-T correlation is primarily due to the meridional advection of both fields, as opposed to direct temperature-dependent chemistry or emissions. Furthermore, the magnitude of the O_3-T regression (dO_3/dT) can be estimated by the ratio of the time-mean O_3 and T meridional gradients. Consideration of expected changes in the meridional gradients of T and O_3 due to climate change indicates that dO_3/dT will likely change, and caution is needed when using the observed climate penalty to predict O_3 changes.

Plain Language Summary

At Earth's surface, ozone is a harmful pollutant. In the summer, we observe higher ozone concentrations on hotter days in many land regions in the midlatitudes. This leads researchers to expect higher ozone concentrations as a result of global warming, based on chemistry that associates higher ozone concentrations with higher temperatures. Here, we show that the relationship between ozone and temperature is largely controlled by atmospheric transport. In particular, north-south movement of air transports both ozone and heat simultaneously. Therefore, the background spatial distributions of ozone and temperature determine how ozone and temperature covary from day to day. The ozone-temperature relationship in the future may look different from today, because global warming is not spatially uniform. We advise caution in using observed ozone-temperature relationship to estimate future ozone changes.

1 Introduction

Ground-level ozone (O_3) is a pollutant harmful to human health and ecosystem productivity (Landrigan et al., 2018; Tai & Val Martin, 2017; Wittig et al., 2007). Observations show that summer O_3 concentrations tend to be higher when temperatures are warmer (e.g., Bloomer et al., 2009; Kerr & Waugh, 2018; Schnell & Prather, 2017). This empirical relationship raises the possibility that a warmer climate would lead to higher O_3 concentrations, which would then require additional emission controls to meet a given

O_3 target (Wu et al., 2008). This increase in O_3 with temperature is referred to as the "ozone-climate change penalty" (or "ozone climate penalty"), and there has been extensive research into the magnitude of this penalty (see Rasmussen et al. (2013) and Fu and Tian (2019) for reviews). A common metric for the ozone climate penalty is the slope of the ozone-temperature (O_3-T) relationship $d\mathrm{O}_3/dT$ (Bloomer et al., 2009), which can be calculated from observations and models. It has been proposed that this metric could be used to predict the impact of future climate warming on ozone. A similar "climate penalty" for fine particulate matter ($PM_{2.5}$) also suggests an increase of $PM_{2.5}$ in a warmer climate (Westervelt et al., 2016; Shen et al., 2017).

However, the use of a climate penalty to predict changes in a future climate requires the assumption that $d\mathrm{O}_3/dT$ (or $d\mathrm{PM}_{2.5}/dT$) does not change with climate. Whether $d\mathrm{O}_3/dT$ is invariant to climate change will depend on the cause of the O_3-T relationship. If the relationship is due to the direct and close to linear temperature dependence of chemical reactions or ozone precursor emissions, it is likely $d\mathrm{O}_3/dT$ will not change with climate. However, if the relationship is caused by an indirect association between O_3 and T, then the relationship may change under a changing climate. Recent studies indicate that the majority of the O_3-T relationship is explained by their indirect association due to atmospheric transport (e.g., Porter & Heald, 2019; Kerr et al., 2019, 2020), suggesting $d\mathrm{O}_3/dT$ will change with the climate. Here, we revisit the processes controlling $d\mathrm{O}_3/dT$, extending the recent studies of Kerr et al. (2020) and Kerr et al. (2021). These studies showed that the O_3-T relationship within midlatitudes is primarily due to jet-induced changes in the surface-level meridional advection of O_3, and spatial variation of the sign of the relationship can be related to changes in the sign of the meridional gradients. We hypothesize that the importance of the surface-level meridional advection holds globally and also applies to temperature, so that $d\mathrm{O}_3/dT$ can be estimated by the ratio of the meridional ozone and temperature gradients.

On the planetary scale, the meridional gradients of scalars such as temperature, specific humidity, and O_3 dominate their zonal gradients. If meridional advection plays the leading role in shaping the large-scale distribution and variability of these scalars, then the tendencies of any two arbitrary scalars x_1 and x_2 are $\partial_t x_1 \approx v\partial_\phi x_1$ and $\partial_t x_2 \approx v\partial_\phi x_2$ (∂_t is partial derivative with respect to time, v is meridional velocity, and ϕ is latitude). This implies

$$\frac{dx_1}{dx_2} \approx \frac{\partial_\phi x_1}{\partial_\phi x_2}, \tag{1}$$

i.e., the relationship between two scalars dx_1/dx_2 can be approximated by the ratio of the x_1 meridional gradients to the x_2 meridional gradients (referred to as the "gradient ratio" below). For the case of O_3 and T this then becomes

$$\frac{dO_3}{dT} \approx \frac{\partial_\phi O_3}{\partial_\phi T}. \tag{2}$$

In this paper, we test this hypothesis first using idealized passive tracers from Kerr et al. (2021) where chemistry is absent, and then in more realistic simulations of O_3. We demonstrate that the spatial pattern and magnitude of dO_3/dT can be quantitatively determined by their gradient ratio $\partial_\phi O_3/\partial_\phi T$ in regions with strong meridional temperature gradients. Furthermore, this framework also applies to explaining the O_3 and specific humidity relationship, as well as the relationship between two chemical tracers with different source regions. We introduce the data sets and methods used in our analyses in Section 2. Next, we test our hypothesis using idealized passive tracer experiments in Section 3, followed by analysis of the ozone-meteorology relationship in Section 4. We then discuss the implications in Section 5 and summarize our results in Section 6.

2 Methods

2.1 GEOS-Chem Idealized Tracers

We analyze simulations of passive tracers with prescribed zonally symmetric emissions using the GEOS-Chem chemical transport model (CTM, v12.0.2) analyzed by Kerr et al. (2021). These simulations are driven by meteorological fields from the Modern Era-Retrospective Analysis for Research and Analysis, Version 2 (MERRA-2) from 2008 to 2010, with a horizontal resolution of 2° latitude×2.5° longitude (∼200×250 km) and 72 vertical levels. Tracers emitted in 10° latitudinal bands have a uniform 50 days^{-1} loss rate. Tracer mixing ratios are denoted $\chi_{\phi_1-\phi_2}$, where ϕ_1 and ϕ_2 are the latitudes of southern and northern emission boundaries. We focus on χ_{40-50} (tracer emitted between 40°–50°N) here to represent midlatitude emissions. We also discuss χ_{20-30} and χ_{60-70} to represent the subtropical and subpolar regions and demonstrate the robustness of our results.

2.2 GMI Ozone Simulations

We also analyze O_3 from simulations of NASA's Global Modeling Initiative chemical transport model (GMI CTM, Duncan et al., 2007; Strahan et al., 2007, 2013) analyzed in Kerr et al. (2020). These simulations are also driven by MERRA-2 fields from 2008 to 2010, with a horizontal resolution of 1° latitude×1.25° longitude (∼100 km) and 72 vertical levels. Early afternoon O_3 (averaged between 1300–1400 hr local time) is analyzed to represent peak daily O_3 concentrations. GMI CTM simulations have demonstrated realistic O_3 variability and its drivers when compared to observations (Strode et al., 2015; Kerr et al., 2019, 2020).

To isolate the role of transport, we also analyze an additional GMI CTM sensitivity simulation from Kerr et al. (2020) where daily variations in natural and anthropogenic emissions and chemistry related processes (e.g., temperature, specific humidity, clouds, etc.) are fixed to monthly mean values. Daily variability in this "transport-only" simulation stems solely from variations in transport (e.g., wind, boundary layer dynamics, etc.).

2.3 Analysis Methods

We focus on the northern hemisphere domain of 10–70°N. The GMI output and MERRA-2 fields are interpolated onto the lower resolution of GEOS-Chem CTM, so that the analysis of the idealized tracers and O_3 is done at the same resolution. We analyze the near-surface (1000–800 hPa) tracer mixing ratios of idealized tracers and O_3 from the model's surface level. We use 2-m daily maximum temperature (T) and 2-m daily-mean specific humidity (Q) from MERRA-2 to represent meteorology. For all fields, daily anomalies are calculated by removing the 2008–2010 monthly climatology at each grid point. Boreal summer (June, July, and August (JJA)) data consist of 276 daily anomalies (concatenating 3 years of JJA data), while boreal winter (December, January, and February (DJF)) data consist of 270 daily anomalies.

Linear least-squares regression between anomalies of tracer concentration and T (or Q) is computed with the Scipy package linregress. Regions with $p > 0.05$ are hatched on maps and defined as not statistically significant. Meridional gradients are calculated by differentiating fields averaged over 2008–2010 JJA (or DJF) with the second order accurate central differences along latitudes. All meridional gradients are then smoothed by a 2-D convolution with a kernel of 10° latitude × 12.5° longitude box for better visualization. The gradient ratios presented are the ratios of the smoothed meridional gradients. Our results are not sensitive to a smaller kernal box.

3 Idealized Passive Tracers

We first consider the relationship between an idealized tracer with a 50 days^{-1} loss rate and zonally symmetric emissions at 40–50°N (broadly the region of ozone precursor emissions) χ_{40-50} and T. Even though there is no direct association between χ_{40-50} and T (i.e., the tracer source and loss rate are independent of temperature), they are significantly correlated on daily timescales as shown by the JJA daily regression $d\chi_{40-50}/dT$ on Figure 1a. There is a prominent spatial pattern where $d\chi_{40-50}/dT$ is positive north of the emission region (40–50°N) and negative south of this region. The absolute values are the highest over midlatitude oceans, but the regression remains significant ($p < 0.5$) over land. Other zonally asymmetric features include the change in signs over main topographic features such as the northern Rockies and the Himalayas.

Next, we look at the meridional gradients of χ_{40-50} and T to determine whether the spatial pattern of gradient ratio $\partial_\phi\chi_{40-50}/\partial_\phi T$ agrees with $d\chi_{40-50}/dT$, as suggested by (1). As the tracer emissions are zonally symmetric, the tracer concentrations are close to being zonally symmetric and highest at the latitudes of emission (see Figure 1 of Kerr et al. (2021)). The meridional gradient of the tracer $\partial_\phi\chi_{40-50}$ is negative to the north and positive to the south of the emission region (Figure 1b contours). In contrast, the meridional temperature gradient $\partial_\phi T$ has the same sign (negative) over most of the Northern Hemisphere, with exceptions for regions of significant topography and near the equator (the peak summer T occurs in the subtropics, Figure 1b shading). As a result, the spatial pattern of their gradient ratio (Figure 1c) is largely consistent with $d\chi_{40-50}/dT$ (Figure 1a), with generally positive values north of the emission region and negative values south of the emissions, except near the equatorial land. However, there are differences in magnitude.

We compute the regional average of $d\chi_{40-50}/dT$ and $\partial_\phi\chi_{40-50}/\partial_\phi T$ to quantitatively compare both quantities and avoid extreme values of $\partial_\phi\chi_{40-50}/\partial_\phi T$ due to local weak temperature gradient (small $|\partial_\phi T|$). We focus on averaging domains of 10° latitude × 20° longitude and calculate the root-mean-square error (RMSE) between the two

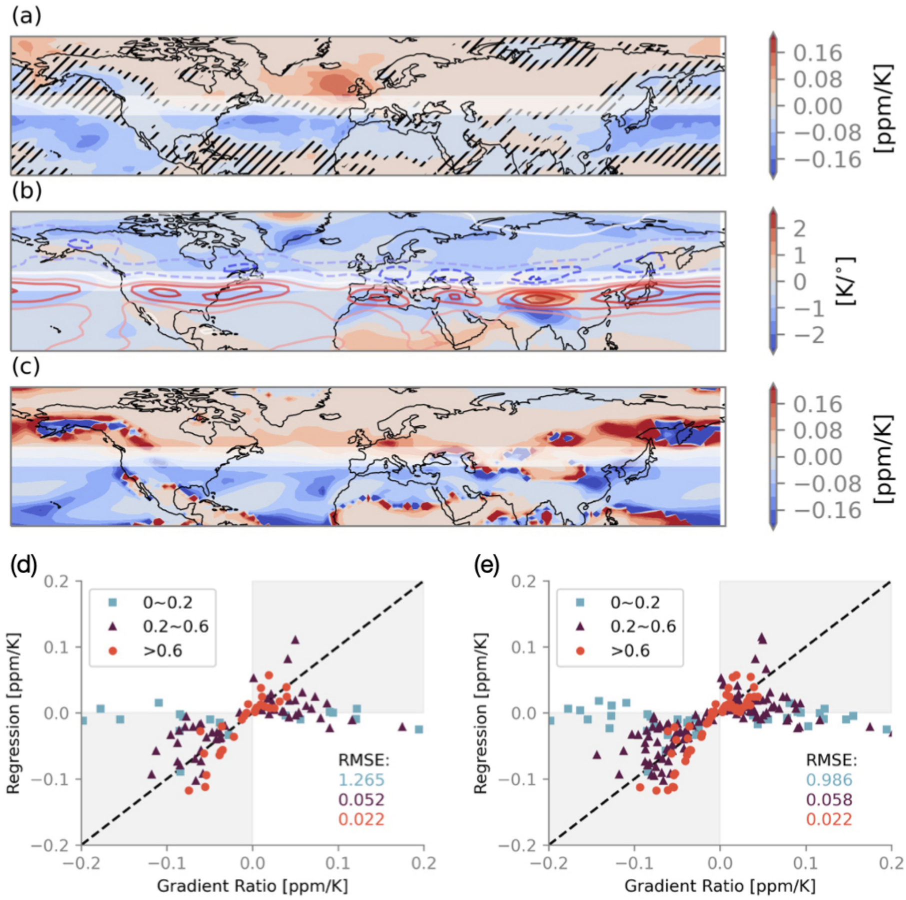

Figure 1. 2008–2010 JJA relationship between idealized tracer emitted from 40–50°N (white bands) χ_{40-50} and daily maximum 2-m temperature T. (a) Daily $d\chi_{40-50}/dT$ regression slope from GEOS-Chem simulation. Regions with $p > 0.05$ (not statistically significant) are hatched. (b) Mean meridional gradient temperature $\partial_\phi T$ in shading and of idealized tracer $\partial_\phi \chi_{40-50}$ in contours (interval of 0.02 ppm/°, positive in solid contours). (c) Gradient ratio $\partial_\phi \chi_{40-50}/\partial_\phi T$. (d) Scatter plot of gradient ratio $\partial_\phi \chi_{40-50}/\partial_\phi T$ versus regression $d\chi_{40-50}/dT$ averaged over 10° latitude × 20° longitude domains, binned by the absolute value of meridional temperature gradient $|\partial_\phi T|$ (K/° in legends). Dashed line shows the 1:1 slope. RMSE between gradient ratio and regression for each $|\partial_\phi T|$ bin is indicated. (e) Same as (d) but averaged over 10° latitude × 10° longitude domains.

quantities to measure the agreement. The agreement between $d\chi_{40-50}/dT$ and $\partial_\phi \chi_{40-50}/\partial_\phi T$ varies with $|\partial_\phi T|$ (Figure 1d). When the meridional temperature gradient is strong ($|\partial_\phi T| >$ 0.6 K/°), the gradient ratio and regression are close to the 1:1 line, and the RMSE is only 0.022 ppm/K (circles). Regions with $|\partial_\phi T| > 0.6$ K/° include northeastern North America, the Mediterranean, northeastern Europe, and central Pacific. In regions with moderate temperature gradients ($0.2 < |\partial_\phi T| < 0.6$ K/°; triangles), the approximation is less accurate (RMSE = 0.052 ppm/K), but we still find agreement between the signs of $d\chi_{40-50}/dT$ and $\partial_\phi \chi_{40-50}/\partial_\phi T$, i.e.,$\partial_\phi \chi_{40-50}/\partial_\phi T$ predicts the sign of $d\chi_{40-50}/dT$. Many land regions (e.g., Europe, western North America, North Africa, northeastern Asia) have moderate meridional temperature gradients. When the temperature gradient is weaker than 0.2 K/° (squares), the regression between χ_{40-50} and T is not significant. Tropical oceans, South Asia, and a part of East Asia fall into this category. This weak relationship is expected: when the temperature gradients are weak the meridional advection of T will only play a minor role in the temperature tendency equation, and the assumption $\partial_t T \approx v \partial_\phi T$ used in deriving (1) is not valid.

To test the sensitivity to the size of the averaging domains, we average over smaller regions of 10° latitude × 10° longitude, and the main results still hold (Figure 1e): RMSE is the largest for the weakest temperature gradients and smallest for the strongest temperature gradients. The same applies for even smaller domains of 5° latitude × 5° longitude.

A similar agreement between the daily regression $d\chi/dT$ and the gradient ratio is found for idealized tracers with different emission regions. For example, Figure 2a shows the comparison between regression and gradient ratio for an idealized tracer with emissions between 20–30°N (χ_{20-30}). The meridional gradient of χ_{20-30} is negative over most of the hemisphere, which results in a generally positive $\partial_\phi \chi_{20-30}/\partial_\phi T$ consistent with the positive $d\chi_{20-30}/dT$. The RMSE between $\partial_\phi \chi_{20-30}/\partial_\phi T$ and $d\chi_{20-30}/dT$ is only 0.015 ppm/K when $|\partial_\phi T| > 0.6$ (circles), but becomes 0.052 ppm/K when $0.2 < |\partial_\phi T| < 0.6$ K/° (triangles). Similarly, the tracer with emissions between 60–70°N (χ_{60-70}) generally has positive $\partial_\phi \chi_{60-70}$ and negative $\partial_\phi \chi_{60-70}/\partial_\phi T$, where we find small RMSE for large $|\partial_\phi T|$ (not shown). All three idealized tracers demonstrate that gradient ratios can robustly approximate the relationship between χ and T on a daily timescale.

The agreement between gradient ratio and $d\chi/dT$ also holds in other seasons. In fact, $|\partial_\phi T|$ in DJF are much stronger than in JJA, and the RMSE between $d\chi_{40-50}/dT$ and $\partial_\phi \chi_{40-50}/\partial_\phi T$ are lower than those in JJA for all three $|\partial_\phi T|$ bins (Figure 2b).

Equation (1) should hold not only for tracer-temperature relationships but also for other meteorological dependencies. One such dependency is specific humidity (Q), and

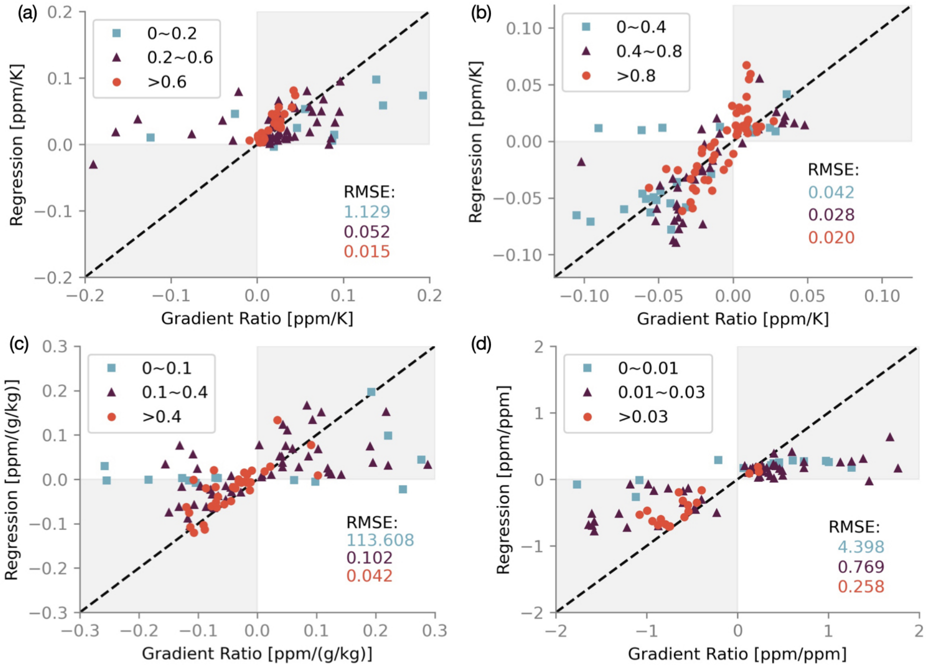

Figure 2. Idealized tracer scatter plots averaged over 10° latitude × 20° longitude regions. (a) JJA gradient ratio $\partial_\phi \chi_{20-30}/\partial_\phi T$ versus regression $d\chi_{20-30}/dT$, binned by their absolute value of meridional temperature gradient (K/°). (b) DJF gradient ratio $\partial_\phi \chi_{40-50}/\partial_\phi T$ versus $d\chi_{40-50}/dT$, binned by their absolute value of meridional temperature gradient (K/°). (c) JJA gradient ratio $\partial_\phi \chi_{40-50}/\partial_\phi Q$ versus $d\chi_{40-50}/dQ$, binned by their absolute value of meridional specific humidity gradient (g/kg/°). (d) JJA gradient ratio $\partial_\phi \chi_{20-30}/\partial_\phi \chi_{40-50}$ versus $d\chi_{20-30}/d\chi_{40-50}$, binned by their absolute value of meridional gradient of $\partial_\phi \chi_{40-50}$ (ppm/°) . Dashed line shows the 1:1 slope. RMSE between gradient ratio and regression for each bin is indicated.

previous studies have found robust relationships between O_3 and Q (e.g., Camalier et al., 2007; Kavassalis & Murphy, 2017; Tawfik & Steiner, 2013). To test this idea, we modify (1) to explore the connection between $d\chi/dQ$ and gradient ratio of specific humidity $\partial_\phi \chi/\partial_\phi Q$. As shown in Figure 2c, the agreement between regression $d\chi_{40-50}/dQ$ and $\partial_\phi \chi_{40-50}/\partial_\phi Q$ is similar to that for the $\chi - T$ relationships. The more visible scatter in Figure 2c is partly due to a more complex spatial pattern of Q in the summer, where specific humidity changes non-monotonically with latitudes on land (discussed further in Section 4).

Another potential application is to use the gradient ratio to explain the regression slope between two chemical tracers, i.e. the relationship between different pollutants with different regional distribution. For example, we can regress the daily concentration of tracers emitted in the subtropics χ_{20-30} onto χ_{40-50}. Figure 2d shows $d\chi_{20-30}/d\chi_{40-50}$ against their gradient ratios $\partial_\phi\chi_{20-30}/\partial_\phi\chi_{40-50}$, scattered around the 1:1 line. Both χ_{40-50} and χ_{20-30} are negatively correlated at 20–50°N, but positively correlated outside of 20–50°N. This pattern occurs because $\partial_\phi\chi_{40-50}$ and $\partial_\phi\chi_{20-30}$ have opposite signs and therefore a negative gradient ratio between the emission regions of the two tracers (20–50°N). Similar to $d\chi/dT$, the RMSE for $\partial_\phi\chi_{20-30}/\partial_\phi\chi_{40-50}$ is the smallest when gradients are strongest ($\partial_\phi\chi_{40-50} > 0.03$ ppm/°, circles). The same applies to χ_{40-50} and χ_{60-70}, where the two tracers are negatively correlated at 40–70°N (not shown). This result suggests our framework can help explain the relationship between different pollutants based on their mean meridional gradients. For example, $PM_{2.5}$ and O_3 have different mean meridional gradients in the southeastern US due to their different spatial distributions (e.g., Schnell & Prather, 2017).

Finally, we examine how well the gradient ratio approximates $d\chi/dT$ during summer (JJA) for tracers with different loss rates. Additional simulations have been performed of tracers with emissions between 40–50°N and loss rates $\tau = 5$, 25, 100, and 150 days^{-1} (Figure S1). Analysis of these simulations shows very little sensitivity to loss rates: for all tracers the gradient ratio performs best when the temperature gradient is the strongest ($|\partial_\phi T| > 0.6$ K/°) and performs poorly at weak temperature gradients ($|\partial_\phi T| < 0.2$ K/°). There is a weak sensitivity in RMSE where smaller RMSEs are found at faster loss rates (Figure S1a). This result is consistent with smaller magnitudes of $d\chi/dT$ for a tracer with a shorter lifetime, so that the absolute errors are smaller.

4 Ozone

We now consider the O_3-T relationship, and whether gradient ratio can also be used to estimate dO_3/dT. The idealized tracer experiments in the previous section illustrated equation (1) in a theoretical context. In this section, we show that these relationships also hold for a tracer (i.e., O_3) with more complex chemistry and with precursors that have spatially variable emissions. As shown in Kerr et al. (2020), there are large spatial variations in the JJA daily correlations between O_3 and T from the GMI simulation, where dO_3/dT is positive over midlatitude land north of ~ 35°N, but negative over the oceans

(Figure 3a). The magnitude of $d\mathrm{O}_3/dT$ over midlatitude land varies, with regions of high values in the northeastern and Midwest US, Continental Europe, and northeastern China. At lower latitudes the sign of $d\mathrm{O}_3/dT$ over land varies, with positive values over central America and northern India, and negative values over northern Africa and southwestern China. A very similar pattern to Figure 3a is found for the GMI "transport-only" simulations from Kerr et al. (2020), indicating (as discussed in Kerr et al. (2020)) that the pattern of $d\mathrm{O}_3/dT$ is primarily a result of atmospheric transport, as opposed to atmospheric chemistry. A similar pattern for the O_3-T relationship is also found in other chemical models (e.g., Meehl et al., 2018; Porter & Heald, 2019; Nolte et al., 2021).

Next, we examine whether these spatial variations in $d\mathrm{O}_3/dT$ can be explained by the gradient ratio $\partial_\phi \mathrm{O}_3/\partial_\phi T$ (equation (2)). To do so, we compare the spatial pattern of JJA meridional gradients of ozone $\partial_\phi \mathrm{O}_3$ and temperature $\partial_\phi T$ in Figure 3b. Ozone concentrations are highest over midlatitude land, resulting in negative $\partial_\phi \mathrm{O}_3$ north of 40°N and positive $\partial_\phi \mathrm{O}_3$ south of 40°N over North America (Figure 3b contours). Over Eurasia, the change of sign of $\partial_\phi \mathrm{O}_3$ occurs at about 35°N. Combined with the negative $\partial_\phi T$ (Figure 3b shading), we expect the $\partial_\phi \mathrm{O}_3$ pattern to yield positive $d\mathrm{O}_3/dT$ north of 35°N according to (2). This is indeed the case, as mentioned above; the only land regions with negative $d\mathrm{O}_3/dT$ are northern Africa and southwestern China. These are regions where $\partial_\phi \mathrm{O}_3$ and $\partial_\phi T$ are positive, so the sign of $d\mathrm{O}_3/dT$ is again consistent with $\partial_\phi \mathrm{O}_3/\partial_\phi T$.

The gradient ratio can also explain the prominent land-sea contrast in the $d\mathrm{O}_3/dT$ pattern. The offshore transport of ozone from the east coasts of North America and Asia leads to strong positive $\partial_\phi \mathrm{O}_3$ on the western ocean basins. This pattern combines with a weak (negative) $\partial_\phi T$ over ocean to result in negative $d\mathrm{O}_3/dT$. Again the sign of $d\mathrm{O}_3/dT$ can also be explained by (2).

To quantify the approximation of (2), we again compare the average regression and gradient ratios over 10° latitude × 20° longitude domains (Figure 3c). Similar to idealized tracers, gradient ratios $\partial_\phi \mathrm{O}_3/\partial_\phi T$ best estimate $d\mathrm{O}_3/dT$ when temperature gradients are strong ($|\partial_\phi T| > 0.6$ K/°). Although the RMSE doubles for moderate temperature gradients ($0.2 < |\partial_\phi T| < 0.6$ K/°), gradient ratio still explains 50% of the $d\mathrm{O}_3/dT$ variance. When temperature gradients are weak ($|\partial_\phi T| < 0.2$ K/°), gradient ratio is not a good predictor of $d\mathrm{O}_3/dT$, though the signs of the two quantities agree more often than not. The same applies to the transport-only simulation (Figure 3c open sym-

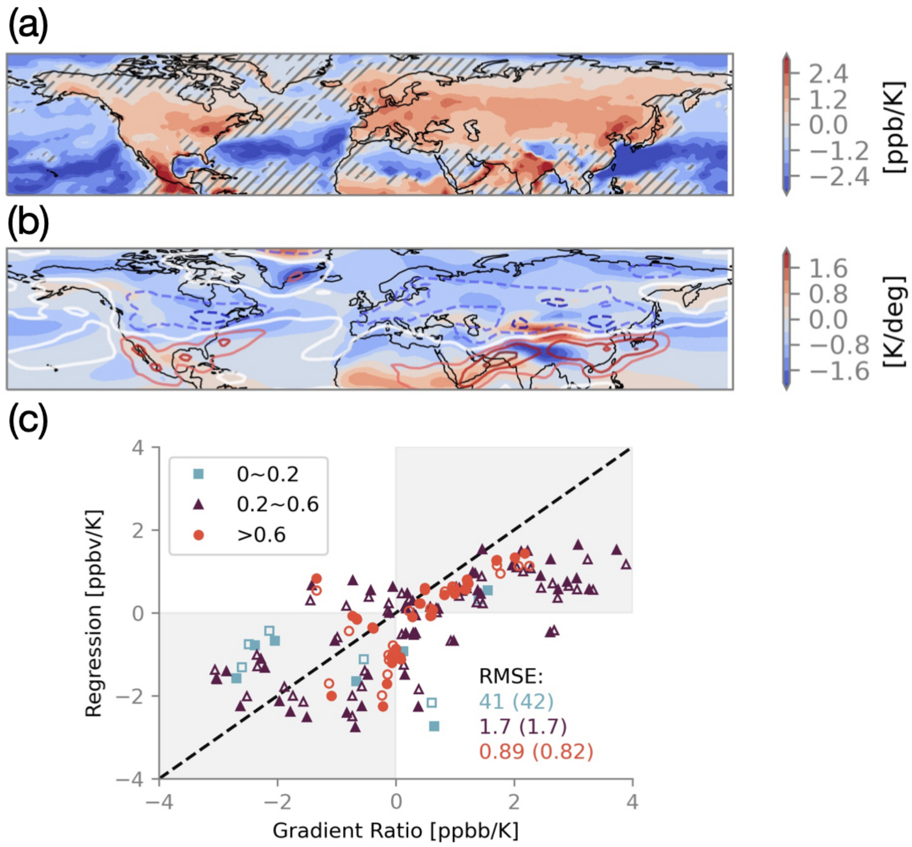

Figure 3. 2008–2010 JJA O_3-T relationship from GMI simulation. (a) Daily dO_3/dT regression slope. Regions with $p > 0.05$ (not statistically significant) are hatched. (b) Mean meridional gradients of $\partial_\phi O_3$ in contours and of $\partial_\phi T$ in shading. Solid contours show positive $\partial_\phi O_3$ and dashed contours show negative $\partial_\phi O_3$, with an interval of 1.0 ppbv/°. (c) Gradient ratio $\partial_\phi O_3/\partial_\phi T$ versus regression dO_3/dT averaged over 10° latitude × 20° longitude regions, binned by the absolute values of meridional temperature gradient $|\partial_\phi T|$ (K/°). Dashed line shows the 1:1 slope. RMSE between gradient ratio and regression for each bin is indicated. Open symbols and RMSE in brackets are from the transport-only simulation.

bols), where we see only slight shifts in dO_3/dT and $\partial_\phi O_3/\partial_\phi T$ and minor differences in RMSE from the control simulation. This result emphasizes the major role of transport and suggests a minor role in chemistry to shape the O_3-T relationship.

There is noticeably more scattering from the 1:1 line for dO_3/dT in Figure 3c than for $d\chi_{40-50}/dT$ in Figure 1c. This difference is not surprising, given that the spatial pattern of O_3 is complex and zonally asymmetric, while χ_{40-50} emissions are zonally uniform. We find that the mismatch between $d\mathrm{O}_3/dT$ and $\partial_\phi \mathrm{O}_3/\partial_\phi T$ is largest near prominent topography (e.g., the Tibetan Plateau) and over oceans away from O_3 sources (e.g., central Pacific). Overall, $\partial_\phi \mathrm{O}_3/\partial_\phi T$ tends to overestimate the magnitude of $d\mathrm{O}_3/dT$.

Similar to what we find earlier with idealized tracers, the gradient ratio allows us to explain not only the O_3-T relationship, but also other meteorological dependencies such as JJA $d\mathrm{O}_3/dQ$. The midlatitude land regions have overwhelmingly positive $d\mathrm{O}_3/dQ$, while significant negative $d\mathrm{O}_3/dQ$ relationships are found in subtropics and most ocean basins (Figure S2a). Southeastern US and China are regions that have either positive or not significant $d\mathrm{O}_3/dT$ but significant $d\mathrm{O}_3/dQ$. Figure S2b shading shows the specific humidity meridional gradient $\partial_\phi Q$, characterized by negative values over many land regions and positive values in central Eurasia, northern Africa, and northwestern North America. Unlike T, Q maximizes locally at midlatitude continental interiors in the summer, leading to a switch in sign of $\partial_\phi Q$. A quantitative comparison between regional $\partial_\phi \mathrm{O}_3/\partial_\phi Q$ and $d\mathrm{O}_3/dQ$ is shown on Figure S2c, binned by their magnitude of meridional specific humidity gradient $|\partial_\phi Q|$. In both the control and transport-only simulations, the gradient ratio $\partial_\phi \mathrm{O}_3/\partial_\phi Q$ can capture $d\mathrm{O}_3/dQ$ well with the smallest RMSE in regions with moderate to strong specific humidity gradients ($|\partial_\phi Q| > 0.1$ g/kg/°). The approximation produces large RMSE when specific humidity gradients are weak ($|\partial_\phi Q| < 0.1$ g/kg/°).

5 Discussion and Possible Implications

As discussed in the Introduction, it is unclear how $d\mathrm{O}_3/dT$ will change with climate. The result that the gradient ratio can be used to approximate $d\mathrm{O}_3/dT$ may provide some useful insight into changes with climate in regions with strong meridional temperature gradients. A robust result of climate projections is polar amplification (Arctic warms more rapidly than lower latitudes), and we expect (on average) that $|\partial_\phi T|$ in mid-latitudes will decrease with increased GHG emissions (Tamarin-Brodsky et al., 2020). This pattern would then result in an increase in the gradient ratio (and $d\mathrm{O}_3/dT$) if there is no change in O_3. However, another robust climate projection is the poleward movement of mid-latitude jet streams. If there is no change in O_3 precursor emissions, the projected northward jet shift in North America will result in $|\partial_\phi \mathrm{O}_3|$ increasing north of the jet (Barnes & Fiore, 2013). An increase in $|\partial_\phi \mathrm{O}_3|$ north of the jet and a decrease in $|\partial_\phi T|$ will both contribute to an increase in the gradient ratio (and $d\mathrm{O}_3/dT$).

Note that Barnes and Fiore (2013) simulation with increasing GHG emissions but constant O_3 precursor emissions show an increase in dO_3/dT north of the jet but decrease south of the jet (see arrows in Figure 3j of Barnes and Fiore (2013)), which is partly consistent with the above arguments on changes in meridional gradients. More detailed analysis of climate projections is needed to determine exactly how the O_3 and temperature gradients as well as dO_3/dT change, and if the changes in gradient ratio explains the change in dO_3/dT. However, our preliminary consideration of expected polar amplification and changes in the jet streams indicates that dO_3/dT will likely change, and caution should be used if predicting the impact of climate warming on O_3 from observed dO_3/dT.

6 Conclusion

Although the temporal correlation between O_3 and T is often explained in terms of the temperature dependence of chemical reactions or emissions, we show here that the dO_3/dT regression is primarily an indirect association due to the meridional advection of both O_3 and T. Further we show that dO_3/dT can be estimated by the ratio of the time-mean O_3 and T meridional gradients (the "gradient ratio"): variations in the gradient ratio explain the opposite signs in dO_3/dT between midlatitude land and ocean, as well as the differences in sign among subtropical land regions. The quantitative accuracy of this approximation (equation (1)) depends on the magnitude of the meridional temperature gradient $|\partial_\phi T|$: it works well when $|\partial_\phi T|$ is strong, but not in regions of weak $|\partial_\phi T|$.

The agreement between the gradient ratio and dO_3/dT provides an approach to understand how dO_3/dT may change with climate. Our preliminary consideration of expected changes meridional gradients of T and O_3 due to polar amplification and jet stream shifts, respectively, indicates that dO_3/dT will likely change, suggesting caution is required if using the present-day dO_3/dT to estimate the impact of climate on O_3. However, further analysis is needed to quantify exactly how meridional gradients and dO_3/dT may change with climate.

The key role of meridional advection, and the agreement between the regression and gradient ratio is a general result. It holds for O_3 with Q, and also for the relationship of idealized tracers (with lifetimes between 5 and 150 days) with T or Q, or between idealized tracers with different source regions. This result suggests that consideration of meridional gradients may provide insights in the relationship between $PM_{2.5}$ and meteorology, as well as the co-occurrence of O_3 and $PM_{2.5}$ pollution events. Future work is planned to explore this possibility.

Acknowledgments

We thank Arlene Fiore, Jean-Francois Lamarque, and Sarah Strode for helpful comments and discussions. This work was funded by support from the US National Science Foundation and the National Aeronautics and Space Administration (NASA).

Data Availability Statement

GEOS-Chem simulations were run on the Maryland Advanced Research Computing Center (MARCC). GEOS-Chem idealized tracer simulation data are available at `https://doi.org/10.6084/m9.figshare.16989856.v1`. NASA GMI CTM output is publicly available on the data portal for the NASA Center for Climate Simulation (`portal.nccs.nasa.gov/datashare/dirac`). NASA's Global Modeling and Assimilation Office and Goddard Earth Sciences Data and Information Services Center (GES DISC) provided and disseminated the MERRA-2 data used in this study, specifically the *inst3_3d_asm_Np* collection (Global Modeling And Assimilation Office (GMAO), 2015).

References

Barnes, E. A., & Fiore, A. M. (2013). Surface ozone variability and the jet position: Implications for projecting future air quality. *Geophysical Research Letters*, *40*(11), 2839–2844. Retrieved 2021-03-01, from `https://agupubs.onlinelibrary.wiley.com/doi/abs/10.1002/grl.50411` doi: https://doi.org/10.1002/grl.50411

Bloomer, B. J., Stehr, J. W., Piety, C. A., Salawitch, R. J., & Dickerson, R. R. (2009). Observed relationships of ozone air pollution with temperature and emissions. *Geophysical Research Letters*, *36*(9). Retrieved 2021-04-23, from `https://agupubs.onlinelibrary.wiley.com/doi/abs/10.1029/2009GL037308` doi: https://doi.org/10.1029/2009GL037308

Camalier, L., Cox, W., & Dolwick, P. (2007). The effects of meteorology on ozone in urban areas and their use in assessing ozone trends. *Atmospheric Environment*, *41*(33), 7127–7137. Retrieved 2021-10-18, from `https://`

www.sciencedirect.com/science/article/pii/S1352231007004165 doi: 10.1016/j.atmosenv.2007.04.061

Duncan, B. N., Strahan, S. E., Yoshida, Y., Steenrod, S. D., & Livesey, N. (2007). Model study of the cross-tropopause transport of biomass burning pollution. *Atmospheric Chemistry and Physics*, *7*(14), 3713–3736. Retrieved 2021-07-27, from https://acp.copernicus.org/articles/7/3713/2007/ (Publisher: Copernicus GmbH) doi: 10.5194/acp-7-3713-2007

Fu, T.-M., & Tian, H. (2019). Climate Change Penalty to Ozone Air Quality: Review of Current Understandings and Knowledge Gaps. *Current Pollution Reports*, *5*(3), 159–171. Retrieved 2021-06-22, from https://doi.org/10.1007/s40726-019-00115-6 doi: 10.1007/s40726-019-00115-6

Global Modeling And Assimilation Office (GMAO). (2015). *MERRA-2 inst3_3d_asm_np: 3d, 3-hourly, instantaneous, pressure-level, assimilation, assimilated meteorological fields v5.12.4.* NASA/GSFC, Greenbelt, MD, USA, NASA Goddard Earth Sciences Data and Information Services Center (GES DISC). Retrieved from https://disc.gsfc.nasa.gov/datacollection/M2I3NPASM_5.12.4.html (NASA/GSFC, Greenbelt, MD, USA, NASA Goddard Earth Sciences Data and Information Services Center (GES DISC). Accessed 07/19/2021) doi: 10.5067/QBZ6MG944HW0

Kavassalis, S. C., & Murphy, J. G. (2017). Understanding ozone-meteorology correlations: A role for dry deposition. *Geophysical Research Letters*, *44*(6), 2922–2931. Retrieved 2021-07-21, from https://agupubs.onlinelibrary.wiley.com/doi/abs/10.1002/2016GL071791 doi: 10.1002/2016GL071791

Kerr, G. H., & Waugh, D. W. (2018). Connections between summer air pollution and stagnation. *Environmental Research Letters*, *13*(8), 084001. Retrieved 2021-06-27, from https://doi.org/10.1088/1748-9326/aad2e2 (Publisher: IOP Publishing) doi: 10.1088/1748-9326/aad2e2

Kerr, G. H., Waugh, D. W., & Miller, S. M. (2021). Jet Stream-Surface Tracer Relationships: Mechanism and Sensitivity to Source Region. *Geophysical Research Letters*, *48*(1), e2020GL090714. Retrieved 2021-02-24, from https://agupubs.onlinelibrary.wiley.com/doi/abs/10.1029/2020GL090714 doi: https://doi.org/10.1029/2020GL090714

Kerr, G. H., Waugh, D. W., Steenrod, S. D., Strode, S. A., & Strahan, S. E.

(2020). Surface Ozone-Meteorology Relationships: Spatial Variations and the Role of the Jet Stream. *Journal of Geophysical Research: Atmospheres*, *125*(21), e2020JD032735. Retrieved 2021-02-24, from https://agupubs.onlinelibrary.wiley.com/doi/abs/10.1029/2020JD032735 doi: https://doi.org/10.1029/2020JD032735

Kerr, G. H., Waugh, D. W., Strode, S. A., Steenrod, S. D., Oman, L. D., & Strahan, S. E. (2019). Disentangling the Drivers of the Summertime Ozone-Temperature Relationship Over the United States. *Journal of Geophysical Research: Atmospheres*, *124*(19), 10503–10524. Retrieved 2021-06-27, from https://agupubs.onlinelibrary.wiley.com/doi/abs/10.1029/2019JD030572 doi: 10.1029/2019JD030572

Landrigan, P. J., Fuller, R., Acosta, N. J. R., Adeyi, O., Arnold, R., Basu, N. N., … Boufford, J. I. e. a. (2018). The Lancet Commission on pollution and health. *The Lancet*, *391*(10119), 462–512. Retrieved 2021-08-09, from https://www.thelancet.com/journals/lancet/article/PIIS0140-6736(17)32345-0/abstract (Publisher: Elsevier) doi: 10.1016/S0140-6736(17)32345-0

Meehl, G. A., Tebaldi, C., Tilmes, S., Lamarque, J.-F., Bates, S., Pendergrass, A., & Lombardozzi, D. (2018). Future heat waves and surface ozone. *Environmental Research Letters*, *13*(6), 064004. Retrieved 2021-03-15, from https://doi.org/10.1088/1748-9326/aabcdc (Publisher: IOP Publishing) doi: 10.1088/1748-9326/aabcdc

Nolte, C. G., Spero, T. L., Bowden, J. H., Sarofim, M. C., Martinich, J., & Mallard, M. S. (2021). Regional Temperature-Ozone Relationships Across the U.S. Under Multiple Climate and Emissions Scenarios. *Journal of the Air & Waste Management Association*. Retrieved 2021-09-10, from https://doi.org/10.1080/10962247.2021.1970048 doi: 10.1080/10962247.2021.1970048

Porter, W. C., & Heald, C. L. (2019). The mechanisms and meteorological drivers of the summertime ozone–temperature relationship. *Atmospheric Chemistry and Physics*, *19*(21), 13367–13381. Retrieved 2021-07-28, from https://acp.copernicus.org/articles/19/13367/2019/ (Publisher: Copernicus GmbH) doi: 10.5194/acp-19-13367-2019

Rasmussen, D. J., Hu, J., Mahmud, A., & Kleeman, M. J. (2013). The

Ozone–Climate Penalty: Past, Present, and Future. *Environmental Science & Technology*, *47*(24), 14258–14266. Retrieved 2021-05-10, from https://doi.org/10.1021/es403446m (Publisher: American Chemical Society) doi: 10.1021/es403446m

Schnell, J. L., & Prather, M. J. (2017). Co-occurrence of extremes in surface ozone, particulate matter, and temperature over eastern North America. *Proceedings of the National Academy of Sciences*, *114*(11), 2854–2859. Retrieved 2021-08-09, from https://www.pnas.org/content/114/11/2854 (Publisher: National Academy of Sciences Section: Physical Sciences) doi: 10.1073/pnas.1614453114

Shen, L., Mickley, L. J., & Murray, L. T. (2017). Influence of 2000–2050 climate change on particulate matter in the United States: results from a new statistical model. *Atmospheric Chemistry and Physics*, *17*(6), 4355–4367. Retrieved 2021-09-15, from https://acp.copernicus.org/articles/17/4355/2017/ (Publisher: Copernicus GmbH) doi: 10.5194/acp-17-4355-2017

Strahan, S. E., Douglass, A. R., & Newman, P. A. (2013). The contributions of chemistry and transport to low arctic ozone in March 2011 derived from Aura MLS observations. *Journal of Geophysical Research: Atmospheres*, *118*(3), 1563–1576. Retrieved 2021-07-27, from https://agupubs.onlinelibrary.wiley.com/doi/abs/10.1002/jgrd.50181 doi: 10.1002/jgrd.50181

Strahan, S. E., Duncan, B. N., & Hoor, P. (2007). Observationally derived transport diagnostics for the lowermost stratosphere and their application to the GMI chemistry and transport model. *Atmospheric Chemistry and Physics*, *7*(9), 2435–2445. Retrieved 2021-07-27, from https://acp.copernicus.org/articles/7/2435/2007/ (Publisher: Copernicus GmbH) doi: 10.5194/acp-7-2435-2007

Strode, S. A., Rodriguez, J. M., Logan, J. A., Cooper, O. R., Witte, J. C., Lamsal, L. N., … Strahan, S. E. (2015). Trends and variability in surface ozone over the United States. *Journal of Geophysical Research: Atmospheres*, *120*(17), 9020–9042. Retrieved 2021-09-17, from https://onlinelibrary.wiley.com/doi/abs/10.1002/2014JD022784 doi: 10.1002/2014JD022784

Tai, A. P. K., & Val Martin, M. (2017). Impacts of ozone air pollution and temperature extremes on crop yields: Spatial variability, adaptation and implications for future food security. *Atmospheric Environment*, *169*, 11–21. Retrieved 2021-08-09, from https://www.sciencedirect.com/science/article/pii/S1352231017305836 doi: 10.1016/j.atmosenv.2017.09.002

Tamarin-Brodsky, T., Hodges, K., Hoskins, B. J., & Shepherd, T. G. (2020). Changes in Northern Hemisphere temperature variability shaped by regional warming patterns. *Nature Geoscience*, *13*(6), 414–421. Retrieved 2021-04-29, from https://www.nature.com/articles/s41561-020-0576-3 (Number: 6 Publisher: Nature Publishing Group) doi: 10.1038/s41561-020-0576-3

Tawfik, A. B., & Steiner, A. L. (2013). A proposed physical mechanism for ozone-meteorology correlations using land–atmosphere coupling regimes. *Atmospheric Environment*, *72*, 50–59. Retrieved 2021-10-18, from https://www.sciencedirect.com/science/article/pii/S1352231013001672 doi: 10.1016/j.atmosenv.2013.03.002

Westervelt, D. M., Horowitz, L. W., Naik, V., Tai, A. P. K., Fiore, A. M., & Mauzerall, D. L. (2016). Quantifying PM2.5-meteorology sensitivities in a global climate model. *Atmospheric Environment*, *142*, 43–56. Retrieved 2021-09-15, from https://www.sciencedirect.com/science/article/pii/S135223101630560X doi: 10.1016/j.atmosenv.2016.07.040

Wittig, V. E., Ainsworth, E. A., & Long, S. P. (2007). To what extent do current and projected increases in surface ozone affect photosynthesis and stomatal conductance of trees? A meta-analytic review of the last 3 decades of experiments. *Plant, Cell & Environment*, *30*(9), 1150–1162. Retrieved 2021-08-09, from https://onlinelibrary.wiley.com/doi/abs/10.1111/j.1365-3040.2007.01717.x doi: 10.1111/j.1365-3040.2007.01717.x

Wu, S., Mickley, L. J., Leibensperger, E. M., Jacob, D. J., Rind, D., & Streets, D. G. (2008). Effects of 2000–2050 global change on ozone air quality in the United States. *Journal of Geophysical Research: Atmospheres*, *113*(D6). Retrieved 2021-05-08, from https://agupubs.onlinelibrary.wiley.com/doi/abs/10.1029/2007JD008917 doi: https://doi.org/10.1029/2007JD008917

Supporting Information for ”Rethinking the Ozone-Climate Change Penalty”

Xiyue Zhang[1], Darryn W Waugh[1], Gaige Hunter Kerr[2] and Scot M Miller[1,3]

[1]Department of Earth and Planetary Sciences, Johns Hopkins University, Baltimore, Maryland, USA

[2]Department of Environmental and Occupational Health, Milken School of Public Health, George Washington University, Washington, DC, USA

[3]Department of Environmental Health and Engineering, Johns Hopkins University, Baltimore, Maryland, USA

Contents of this file

1. Figures S1 to S2

Introduction

We include additional figures in support of and are referenced in the main manuscript.

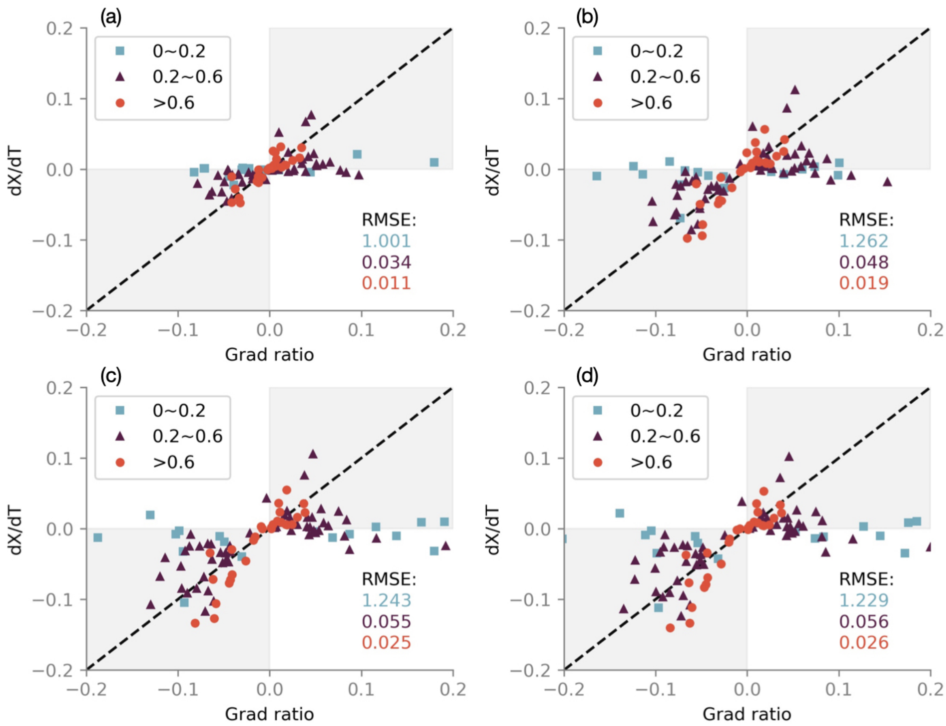

Figure S1. Idealized tracer scatter plots of JJA gradient ratio $\partial_\phi \chi_{40-50}/\partial_\phi T$ versus $d\chi_{40-50}/dT$ averaged over 20° longitude × 10° latitude regions with loss rate of (a) 5 days^{-1}, (b) 25 days^{-1}, (c) 100 days^{-1}, and (d) 150 days^{-1}. All points are colored by their absolute value of meridional temperature gradient. Dashed line shows the 1:1 slope. RMSE between gradient ratio and regression for each bin is indicated.

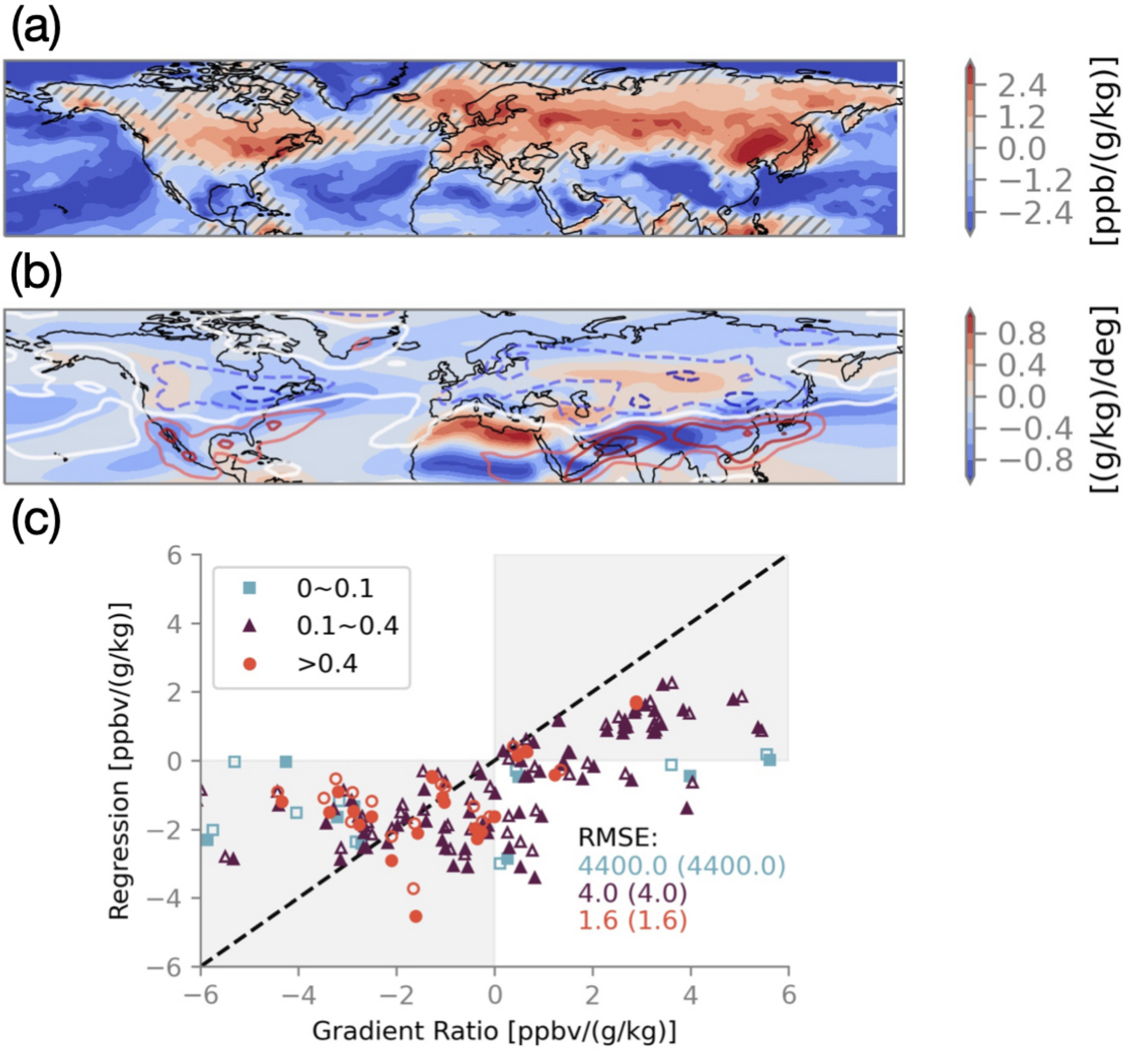

Figure S2. 2008–2010 JJA O_3-Q relationship from GMI simulation. (a) Daily dO_3/dQ regression slope. Regions with $p > 0.05$ (not statistically significant) are hatched. (b) Mean meridional gradients of $\partial_\phi O_3$ in contours and of $\partial_\phi Q$ in shading. Solid contours show positive $\partial_\phi O_3$ and dashed contours show negative $\partial_\phi O_3$, with an interval of 1.0 ppbv/°. (c) Gradient ratio $\partial_\phi O_3/\partial_\phi Q$ versus regression dO_3/dQ averaged over 10° latitude × 20° longitude regions, binned by the absolute values of meridional temperature gradient $|\partial_\phi Q|$ (g/kg/°). Dashed line shows the 1:1 slope. RMSE between gradient ratio and regression for each bin is indicated. Open symbols and RMSE in brackets are from the transport-only simulation.